

# Microfluidic Model Porous Media: Fabrication and Applications

Alimohammad Anbari, Hung-Ta Chien, Sujit S. Datta,\* Wen Deng, David A. Weitz, and Jing Fan\*

Complex fluid flow in porous media is ubiquitous in many natural and industrial processes. Direct visualization of the fluid structure and flow dynamics is critical for understanding and eventually manipulating these processes. However, the opacity of realistic porous media makes such visualization very challenging. Micromodels, microfluidic model porous media systems, have been developed to address this challenge. They provide a transparent interconnected porous network that enables the optical visualization of the complex fluid flow occurring inside at the pore scale. In this Review, the materials and fabrication methods to make micromodels, the main research activities that are conducted with micromodels and their applications in petroleum, geologic, and environmental engineering, as well as in the food and wood industries, are discussed. The potential applications of micromodels in other areas are also discussed and the key issues that should be addressed in the near future are proposed.

## 1. Introduction

Microfluidic model porous media, better known as micromodels, are devices with a transparent connected porous network, which enables the direct visualization of the complex fluid flow dynamics occurring inside. Complex fluid flow in porous media is ubiquitous in natural processes and engineering systems. Examples include, but are not limited to, the multiphase flow in oil recovery,<sup>[1]</sup> subsurface water flow and solute

transport,<sup>[2]</sup> gas or aqueous vanadium redox species flow through porous electrodes in fuel cells,<sup>[3]</sup> and interstitial flow in biological tissues.<sup>[4]</sup> As a result of the drastic reduction in the characteristic length of the system to the micrometer/nanometer scale, interfacial forces play a dominant role in governing the fluid flow physics.<sup>[5]</sup> As such, the flow behavior deviates from what is predicted in the length scale larger than the micrometer/nanometer scale. To effectively study the flow mechanisms, a direct visualization of the fluid structure and flow dynamics inside the media is a key; however, since real porous media are not transparent to visible light, such visualization is challenging. Advanced imaging techniques, such as focused ion beam scanning electron microscopy (FIB/SEM)

and X-ray microcomputed tomography (micro-CT), have been used extensively to extract 2D or 3D high-resolution static images of the inner porous structure.<sup>[6]</sup> However, the long scanning time (on the order of minutes or even hours) often deprives researchers of studying the pore-scale dynamics of the flow, although developing faster versions of these imaging approaches is an active area of work.<sup>[7]</sup> An alternative approach is to use magnetic resonance imaging, which can provide measurements of faster dynamics, but is often limited in spatial resolution.<sup>[8]</sup>

Micromodels allow for a pore-level observation of the flow and the fluid structure under transient conditions by integrating them with a microscope and a camera.<sup>[1e,2b,9]</sup> The micromodels are made of optically transparent materials, such as glass and some transparent polymers, and can be fabricated by a variety of nonadditive and additive manufacturing techniques, or by packing particles such as glass beads.<sup>[2b,9]</sup> Depending on the fabrication method, the micromodel possesses either a 2D or 3D porous structure. A 2D micromodel consists of single-layer microfluidic channels with an arbitrary porous structure. Therefore, the complex flow behavior in 2D micromodels can be easily observed with an optical microscope. However, the 2D micromodel is not able to capture the physics associated with the porous connection in the third dimension, which is sometimes a critical feature for the flow in porous media; for example, the breakup of immiscible fluids is reduced in 3D due to the enhanced connectivity and tortuosity of the pore space.<sup>[10]</sup> A 3D micromodel can thus better mimic the 3D geometric features of realistic porous media, although visualization in 3D micromodels requires a close match of

A. Anbari, H.-T. Chien, Prof. J. Fan  
 Department of Mechanical Engineering  
 The City College of New York  
 New York, NY 10031, USA  
 E-mail: jfan1@ccny.cuny.edu

Prof. S. S. Datta  
 Department of Chemical and Biological Engineering  
 Princeton University  
 Princeton, NJ 08544, USA  
 E-mail: ssdatta@princeton.edu

Prof. W. Deng  
 Department of Civil, Agriculture, and Environmental Engineering  
 Missouri University of Science and Technology  
 Rolla, MO 65409, USA

Prof. D. A. Weitz  
 Department of Physics and School of Engineering and Applied Sciences  
 Harvard University  
 Cambridge, MA 02138, USA

 The ORCID identification number(s) for the author(s) of this article can be found under <https://doi.org/10.1002/sml.201703575>.

DOI: 10.1002/sml.201703575

the refractive index for both solid matrix and fluids. Moreover, for any type of micromodel, approaches are available to tailor the surface properties, such as the wettability to a certain fluid. Since the development of the first micromodels in the 1950s,<sup>[11]</sup> a wide variety of 2D and 3D micromodels have been established to study flow and transport phenomena in porous media. The studies are based on the direct observation of the pore-scale and/or macroscale fluid structures, the flow field visualization, and the characterization of matrix–fluid interactions. These studies have been greatly beneficial to the petroleum, geologic, and environmental engineering.

In this work, we present a detailed, systematic review on the fabrication and applications of both 2D and 3D micromodels. We will introduce the most commonly used materials and their properties, and the existing fabrication methods. We also discuss some promising, well-developed microfabrication methods that can be potentially used in the future. Moreover, we present a detailed discussion on the applications of micromodels, by summarizing and categorizing the research efforts on studying flow and transport phenomena in micromodels, with an emphasis on fundamental scientific research. We hope this summary could benefit a large audience situated across assorted areas involving flow and transport in porous media. Finally, we will propose some new topics that can potentially benefit from the micromodel technique.

## 2. Materials

To directly visualize the fluid flow within a micromodel, the model porous media should be optically transparent. Available economic options include glass, silicon, and some polymer materials such as polydimethyl siloxane (PDMS) and polymethyl methacrylate (PMMA). These materials have different mechanical, thermal, and chemical properties, and suit different fabrication methods. In this section, we will discuss the properties of each of the materials commonly used for making micromodels.

### 2.1. Nonorganic Materials

Glass and silicon are two nonorganic materials that have been widely used to fabricate micromodels. Since silicon is not transparent for visible light, the silicon micropattern is usually bound with a glass plate, through which the internal flow can be observed under a microscope.<sup>[12]</sup> The Young's modulus of glass is 50–90 GPa and silicon is 130–180 GPa.<sup>[13]</sup> Because of the high stiffness, glass- and silicon-based micromodels can well maintain their original structure, even at high-load conditions. This feature makes them a great candidate for the experiments involving high fluid pressure, e.g., flow visualization in a multiphase high-pressure flow of supercritical CO<sub>2</sub> and water.<sup>[14]</sup> Moreover, glass and silicon can withstand temperatures as high as 550 and 1400 °C, respectively,<sup>[15]</sup> and are compatible with many solvents.<sup>[13,16]</sup> Therefore, the resultant micromodels are best suited for performing flow experiments under harsh thermal and/or chemical conditions, such as studying two-phase flow at reservoir conditions using crude oil.<sup>[17]</sup>



**Alimohammad Anbari** is a Ph.D. student in Mechanical Engineering at the City College of New York. He obtained his Master's degree at Sharif University of Technology and his Bachelor's degree at Iran University of Science and Technology. His main research interests lie in the area of microfluidics ranging from the theory to the design and applications. More specifically, his work investigates the use of microfluidics as a powerful tool for simulating and understanding transport phenomena in biological tissues.



**Sujit Datta** is an Assistant Professor of Chemical and Biological Engineering at Princeton University. His research focuses on understanding and controlling the multiscale interactions between soft materials and their complex environments, motivated by problems in energy, biotechnology, and environmental science. He

earned his Ph.D. in Physics from Harvard University and did postdoctoral research in Chemical Engineering at the California Institute of Technology before joining Princeton.



**Jing Fan** is an Assistant Professor of Mechanical Engineering at the City College of New York. Her group is researching on a variety of transport phenomena in porous media, ranging from subsurface environment to biological tissues, using microfluidics as an important tool. She also aims at advancing the

microfluidic technology and promoting its applications in the development of new materials and structures. Before joining CCNY she conducted her postdoctoral research in Applied Physics at Harvard University and obtained her Ph.D. in Mechanical Engineering at The University of Hong Kong.

In addition, the surface wettability of glass and/or silicon can be easily modified by methods like silanization reaction,<sup>[18]</sup> surface coating,<sup>[19]</sup> and layer-by-layer electrolyte deposition.<sup>[20]</sup> The ease of surface treatment aids in the investigation on the effect

of wettability on porous media flow, which is crucial to understanding many petroleum and environmental engineering processes.<sup>[21]</sup> The unique mechanical, thermal, and chemical properties of glass and silicon require one to use etching or laser engraving to create the porous microstructures on the bulk material.<sup>[22]</sup> These approaches are usually more complex, expensive, and hazardous than those for processing soft materials. To ensure the structural integrity of the micromodels at high pressures, special sealing/bonding processes are also needed. The bonding methods include the field-assisted thermal bonding,<sup>[23]</sup> fusion bonding,<sup>[24]</sup> calcium-assisted bonding,<sup>[25]</sup> low-temperature bonding,<sup>[26]</sup> and finally the adhesive bonding.<sup>[27]</sup> Another way of constructing micromodels with truly 3D structures is by packing uniformly sized or multiply sized glass beads within a microfluidic channel. The 3D bead-packed micromodels maintain the superiority of glass mechanical, thermal, and chemical properties, with a relatively simple fabrication process. However, the visualization of flow in such 3D micromodels requires a close match of the refractive index for the fluids and glass.<sup>[10,28]</sup>

## 2.2. Polymeric Materials

Characterized by optical transparency, moderate chemical resistance, and low cost of fabrication, some elastomer and thermoplastic materials have attracted much attention in fabricating micromodels. There is also a great potential in production scale-up for polymer-based micromodels. PDMS and PMMA are the two most commonly used polymers in this regard. Both have been extensively used to fabricate 2D micromodels.<sup>[2b,29]</sup> By binding multiple-layer polymer patterns or 3D printing, 3D micromodels have also been developed with these two materials.<sup>[30]</sup>

PDMS is an elastomer that is ideal for rapid replication of fine structures by soft lithography micromolding, and thus has been widely used to fabricate microfluidic devices, including micromodels.<sup>[2b,30c,31]</sup> Depending on the monomer–crosslinker ratio and curing temperature, Young's modulus of the resultant PDMS can be tuned over a wide range, from 1.3 to 3 MPa.<sup>[32]</sup> It is transparent in the UV–visible light spectrum with a refractive index of around 1.41.<sup>[33]</sup> Notably, the good permeability of PDMS to oxygen and carbon dioxide makes it well suited for cell-culture-involved applications. Hydrophobic PDMS can be treated to be hydrophilic by plasma oxidation,<sup>[34]</sup> UV-induced graft polymerization of poly(acrylic acid),<sup>[35]</sup> or polyelectrolyte multilayer coating.<sup>[36]</sup> In addition, PDMS can be easily bound with glass or PDMS, which further simplifies the construction of PDMS-based micromodels. However, PDMS swells in contact with nonpolar solvents (such as hydrocarbons, toluene, and dichloromethane) and thus cannot be used for manipulations involving these solvents.<sup>[37]</sup> The “aging effect,” characterized by a slow and irreversible alteration of the chemical, mechanical, and thermal properties over time, is another disadvantage of this material, which could eventually lead to malfunctioning of the devices.<sup>[38]</sup>

PMMA is a thermoplastic material that has been used to fabricate micromodels.<sup>[29a,c,30b,39]</sup> The Young's modulus of PMMA varies in the range of 1.8–3.1 GPa,<sup>[16,40]</sup> so the stiffness of PMMA falls in between that of glass and PDMS. PMMA usually maintains its structure well during ordinary flooding

experiments. The chemical resistance of PMMA is better than PDMS, but not comparable with glass. At room temperature, it is resistant to most inorganic chemicals, aliphatic hydrocarbons, fats and oils, alkalis solutions, and diluted acids.<sup>[41]</sup> However, it can be dissolved by many common organic solvents like ethanol, dimethyl sulfoxide (DMSO), and acetone. As a clear resin, PMMA can be easily processed by stereolithography to generate 3D microstructures;<sup>[42]</sup> however, the resolution of the features generated by regular additive manufacturing methods is less than that by nonadditive manufacturing.<sup>[43]</sup> The wetting property of PMMA surface can be treated by plasma treatment,<sup>[44]</sup> UV/ozone exposure,<sup>[45]</sup> nitric acid oxidation,<sup>[45]</sup> or polymer coating.<sup>[45]</sup>

## 3. Fabrication

The fabrication of 2D and 3D micromodels can be implemented by either nonadditive manufacturing or additive manufacturing, with the exception of directly packing microparticles to form the 3D model porous media. In the following, we will discuss the procedure and characteristics of each method.

### 3.1. Nonadditive Manufacturing

Despite the variety of materials used for making micromodels, almost all nonadditive manufacturing approaches involve two main steps: (1) lithography, which transfers the predesigned geometric pattern from a mask to a photoresist layer on the substrate; and (2) shaping, which gives a particular shape to the micromodel material by, for example, etching, replica molding, and hot embossing. The most widely used lithography technique for micromodel fabrication is photolithography, which applies UV to facilitate the pattern formation on the photoresist. The combination of photolithography and replica molding is more commonly referred to as “soft lithography,”<sup>[46]</sup> because it is used to process soft elastomers, like PDMS.

#### 3.1.1. Photolithography

We will now describe the process of photolithography. First, a photomask is printed with a laser printer based on a computer-aided design. To transfer the pattern of the mask to a photoresist layer, the layer will be spin-coated onto a substrate that can be a silicon wafer or the micromodel material to be processed. The thickness of the layer depends on the viscosity of the photoresist and the spinning speed. Then, the substrate is placed on a hot plate or in an oven to remove the volatile solvents in the photoresist; this step is called “soft baking” or “prebaking.” The photoresist layer will then be exposed to UV light through the mask, which changes the properties of the exposed material. Depending on the type of photoresist (positive or negative) either the exposed or nonexposed area can then be washed away by a developer solution. For the negative photoresist, a postexposure baking may be needed before the development to accelerate the photoresist polymerization. **Figure 1** illustrates the procedure of photolithography.



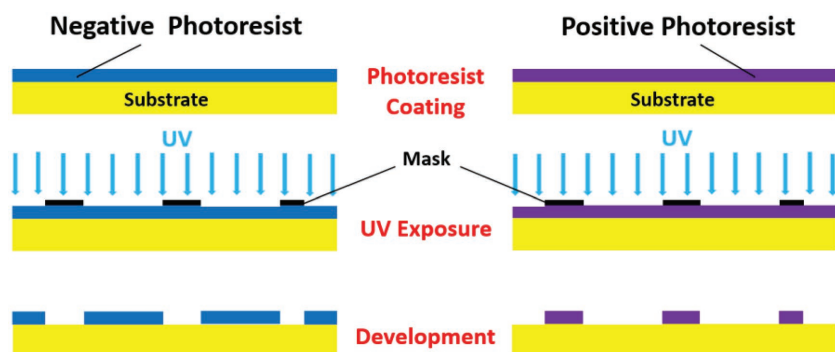


**Figure 1.** Simplified illustration of the photolithography process using positive or negative photoresists: spin-coating a photoresist layer with controllable thickness on a substrate; UV exposure through a mask with predesigned patterns; photoresist developing using a developer solution. Prebake or postbake is not illustrated.

In most cases, the photoresist master mold will be used as the patterned template for the replica molding of PDMS. Sometimes the master mold itself is directly used to bind with a flat plate, such as a glass plate, to construct the model porous medium.<sup>[47]</sup> Although this is not time- or cost efficient, photoresist has higher stiffness than PDMS and therefore less likely to deform. **Figure 2** shows several typical regular and irregular patterns of the 2D porous structures by photolithography, including crosshatched grid,<sup>[48]</sup> pore body–throat network,<sup>[49]</sup> regular arrays of pillars,<sup>[12]</sup> irregular interconnected channels,<sup>[50]</sup> and irregular pattern inspired from the structure of a real porous rock.<sup>[51]</sup>

### 3.1.2. Shaping

If the micromodel is made of glass or silicon and therefore processed by etching, the substrate on which photoresist is deposited is actually the micromodel material. Following the

photoresist development, dry, wet, or a combination of both etching techniques will be used to remove the material not protected by the photoresist. If the micromodel is made of PDMS and therefore can be processed by replica molding, the substrate on which photoresist is deposited is usually a silicon wafer. If the micromodel is made of the thermoplastic PMMA, hot embossing can be used to form the microstructure. In the following, we will introduce etching, replica molding, and hot embossing techniques in more details.

**Etching:** This refers to the removal of the material unprotected by the photoresist layer. If it involves the usage of liquid chemicals or etchants to remove the material, it is called “wet etching.” If it involves the exposure of material to a plasma of reactive gases, such as fluorocarbons, oxygen, chlorine, and boron trichloride, it is called “dry etching.”<sup>[22a,b]</sup> As a powerful material-removal technique, etching can be used to process rigid and brittle materials like glass and silicon, as well as soft materials like PDMS.<sup>[52]</sup>

Wet etching makes use of chemical reactions between the etchants and the material. Common etchants include buffered hydrofluoric acid (BHF); a mixture of HF and hydrochloric acid (HCl); a mixture of hydrochloric, nitric, and acetic acid (HNA);<sup>[53]</sup> and potassium hydroxide (KOH). BHF is most commonly used for etching glass, and HNA and KOH are commonly used for silicon. It should be noted that ordinary photoresists are sufficiently stable against corrosive acid etchants, so they serve to selectively protect a micromodel pattern from acid etching. In the case that a photoresist is insufficient (such as a fabrication that involves deep etching in glass), a metallic coating of Cu, Cr, and Ag can be used as the protector.<sup>[54]</sup> Thus, by submerging into the etchant solution, the exposed material will react with the etchant and be etched away. The etching rate can be adjusted through reaction time, temperature, and

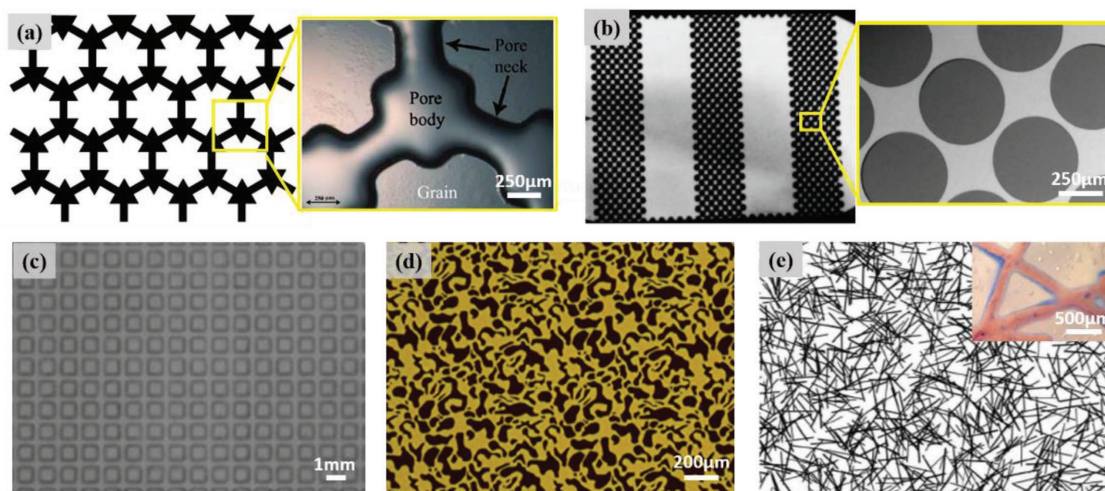


**Figure 2.** Regular and irregular patterns of the 2D porous structures by photolithography: a) pore body–throat network, reproduced with permission,<sup>[49]</sup> Copyright 2011, Elsevier; b) regular arrays of pillars, reproduced with permission,<sup>[12]</sup> Copyright 2012, Royal Society of Chemistry; c) cross-hatched grid, reproduced with permission under a CC-BY Creative Commons license,<sup>[48]</sup> Copyright 2017, Elsevier; d) irregular pattern representing the structure of a thin layer of real rock, reproduced with permission,<sup>[51]</sup> Copyright 2014, Elsevier; and e) irregular interconnected channels, reproduced with permission.<sup>[52]</sup> Copyright 2007, Elsevier.

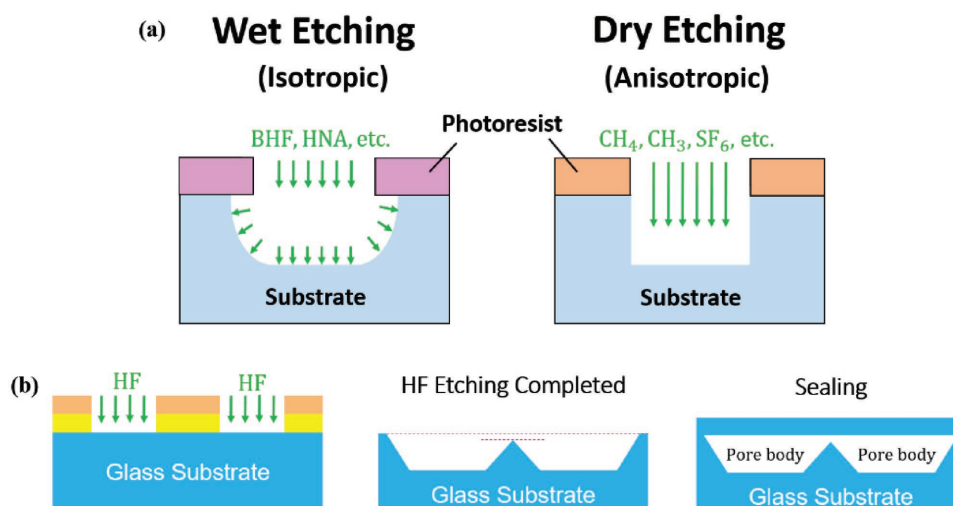


**Figure 3.** The schematic illustration of a) the isotropic wet etching and anisotropic dry etching, and b) the etching and sealing processes in fabricating 2.5D glass micromodel. Adapted with permission.<sup>[56]</sup> Copyright 2017, Royal Society of Chemistry.

the compositions and concentrations of the etchant solution. The main drawback of wet etching is due to the isotropy of chemical reactions—the etchant can penetrate underneath the mask, which prevents the formation of perfectly vertical walls, as demonstrated by **Figure 3a**.<sup>[55]</sup>

A recent advance is the fabrication of “2.5D” micromodels using HF etching, which leverages the trapezoidal channel cross section formed during wet etching to design connected microchannels.<sup>[56]</sup> In this approach, the neighboring channels (the pore “bodies”) are etched so that their trapezoidal cross sections begin to overlap; controlling the amount of overlap controls the depth of this pore “throat.” **Figure 3b** illustrates this process. Therefore, these micromodels enable more geometrical complexity to be incorporated in a 2D device.

Dry etching makes use of the high kinetic energy of particle beams to destroy and remove material. Among the various types of beams, reactive-ion beam has been widely used. The reactive-ion etching process consists of three steps: (1) adsorption of reactive radicals on the surface; (2) a chemical reaction between the radicals and surface; and (3) desorption of the reaction production in the form of volatile species or precursors.<sup>[57]</sup> In some other dry-etching processes, high-energy particles attack the material and cause the atoms on the surface to be evaporated directly without any chemical reactions being involved.<sup>[58]</sup> Compared to wet etching, dry-etching techniques allow for better control on the etching direction, which results in straight walls;<sup>[59]</sup> however, dry etching requires sophisticated facilities and therefore is more expensive than wet etching. Moreover, the rate of dry etching on glass or silicon is below  $1 \mu\text{m min}^{-1}$ , significantly slower than the rate of wet etching, which can reach the order of magnitude of  $10 \mu\text{m min}^{-1}$ .<sup>[60]</sup> **Figure 3a** illustrates the processes of dry and wet etching. The wrinkles shown in the zoom-in SEM image in **Figure 4a** implies the curved channel walls of the glass-based micromodel by wet etching; the zoom-in SEM image in **Figure 4b** clearly shows the sharp straight channel walls of the silicon-based micromodel by dry etching.<sup>[55,61]</sup>

**Replica Molding:** This shapes polymer materials using a mold in the negative shape of the micropattern; the mold can be, for

example, the combination of the substrate and the photoresist after development from the lithography process. The mold will then be filled with the prepolymer material. The prepolymer is then crosslinked and peeled from the mold. With the replica-molding approach, the structure can be conveniently copied dozens of times using the same mold. At last, the crosslinked polymer will be bound with another polymer or glass plate to complete the whole micromodel device. Over the past decades, 2D PDMS micromodels with a variety of single-layer porous structures have been fabricated by combining lithography and replica molding, or so-called “soft lithography.”<sup>[46]</sup> **Figure 4c** shows the SEM image of a PDMS-based 2D micromodel with the pillar-array pattern.<sup>[29d]</sup> By making porous structures with variable depth or binding together multiple layers of microstructures, 3D micromodels have also been constructed.<sup>[30c]</sup>

Besides, being used as the micromodel material directly, the PDMS patterns have also been used as a mold to replicate Norland Optical Adhesive 81 (NOA81) patterns. The NOA81 pattern is then bound to another layer of NOA81 to form the micromodel.<sup>[62]</sup> The wettability of the NOA81 micromodel can be modified by exposing to high-energy UV radiation, applying chemical vapor deposition, and soaking NOA81 samples in brine and crude oil for several hours.<sup>[62]</sup> By doing the extra replica molding, the possibility of damaging the original photoresist mold due to repeated use is minimized. Therefore, this strategy could potentially be more efficient since the fabrication of the photoresist mold is time consuming. The resultant NOA81 micromodel has been used to study the effect of wettability on controlling displacement patterns for a multiphase flow in porous media.<sup>[62]</sup>

**Laser Engraving:** Micropatterns can also be directly engraved onto a substrate using laser technology. This approach can generate micropatterns on a variety of materials, including glass, silicon, PMMA, and PDMS. More importantly, it can be implemented with two simple steps to draw the pattern and engrave without needing to make any extra components. However, this technique is also accompanied by several drawbacks. First, the typical resolution of laser engraving is below 1000 dpi;<sup>[22c]</sup> in comparison, the typical resolution of photolithography



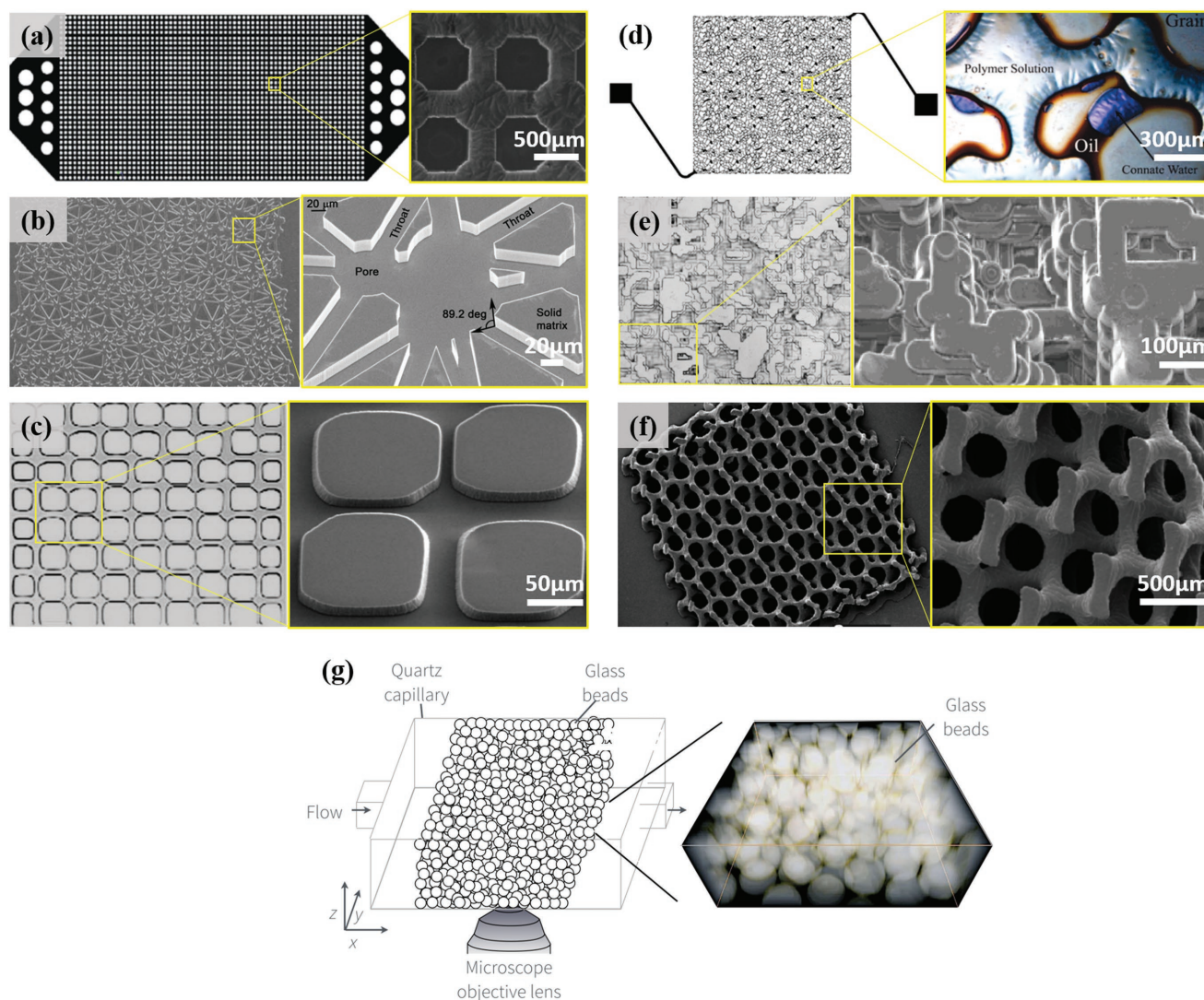


**Figure 4.** Microscopy images of micromodels fabricated by different methods. a) 2D glass micromodel by wet etching. Reproduced with permission.<sup>[55]</sup> Copyright 2011, Elsevier. b) 2D silicon micromodel by dry etching. Reproduced with permission.<sup>[61]</sup> Copyright 2011, Royal Society of Chemistry. c) 2D PDMS micromodel by soft lithography. Reproduced with permission.<sup>[29d]</sup> Copyright 2004, American Geophysical Union. d) 2D glass micromodel by laser engraving. Reproduced with permission.<sup>[22c]</sup> Copyright 2013, Taylor & Francis Group, LLC. e) 3D PMMA micromodel by hot embossing. Reproduced with permission.<sup>[29a]</sup> Copyright 2012, ASME. f) 3D PDLLA 3-FAME/NVP porous structure by stereolithography. Reproduced with permission.<sup>[69]</sup> Copyright 2009, American Chemical Society. g) 3D micromodel by packing glass beads. Adapted with permission.<sup>[10]</sup> Copyright 2013, American Institute of Chemical Engineers. The zoom-in images in panels (d) and (g) are from optical microscopy and confocal microscopy, respectively. All the other images are SEM images. Panel (g) also shows the reconstructed 3D structure of the bead pack.

masks used for fabricating micromodels is one order of magnitude higher. Second, the engraving speed decreases with the resolution; the speed is on the order of magnitude of  $1\text{--}10\text{ m min}^{-1}$ .<sup>[22c]</sup> Figure 4d shows the microscopy image of a laser-engraved micromodel at the pore-scale.<sup>[22c]</sup>

**Hot Embossing:** Thermoplastic polymers, such as PMMA, are well known for maintaining their chemical and physical integrity under high-pressure and high-temperature conditions. This unique ability allows for various activities, such as softening, reshaping, or even melting processes to be performed on thermoplastic polymers with excellent stability over a wide range of operational pressures and temperatures.<sup>[63]</sup>

Hot embossing imprints the desired patterns by stamping the pattern on a thermoplastic polymer substrate during a controlled high-temperature and high-pressure condition. By softening the material at high temperature, the required force to reshape the material into the stamp become minimized. Like replica molding, one-time fabrication of a master is required, but once the master is generated, it can be used to transfer desired microstructures by the hot-embossing process. Generally, the hot-embossing technique can be broken down into four categories, including heating, embossing, cooling, and demolding.<sup>[39]</sup> Figure 4e shows 3D PMMA micromodel fabricated by hot embossing.

Besides the methods discussed above, mechanical processing, as a well-developed microfabrication technique, can be potentially used for fabricating micromodels.<sup>[64]</sup> This method uses tool bits to remove the material. Since the movement of the tool bit can be accurately controlled, no protective layer is needed.

### 3.2. Additive Manufacturing

Stereolithography is a form of additive manufacturing, or 3D printing, and has been used to construct 2D micromodels with either constant or variable channel height for studying the displacement pattern in drainage and foam flooding enhanced oil recovery (EOR).<sup>[48,65]</sup> Stereolithography is based on the spatially controlled solidification of a liquid resin by photopolymerization. Liquid resin is deposited layer by layer onto a position-controllable stage. After depositing each layer, a computer-guided laser beam illuminates the desired pattern on that layer following a specific path. After completing the deposition and illumination of all layers, the un-crosslinked resin is washed away to form the desired 3D porous structure.<sup>[2b]</sup>

Besides stereolithography, other additive manufacturing methods include fused deposition,<sup>[66]</sup> laser sintering,<sup>[67]</sup> and electron-beam melting.<sup>[68]</sup> All these methods involve the solidification of liquid or melted material to form the hard material with the predesigned structure. Although additive manufacturing has been widely used to construct 3D structures of a variety of materials, such as resin, metal, concrete, and hydrogel, its application in making micromodels is still in an early stage.<sup>[43]</sup> With the selection of optically transparent addible materials becoming larger, this method can be very promising in constructing micromodel for flow-related study. Figure 4f shows the SEM images of a porous scaffold made of PDLLA 3-FAME/NVP (fumaric acid monoethyl ester functionalized 3-armed poly(D,L-lactide) oligomers using N-vinyl-2-pyrrolidone) resin by stereolithography; due to the high water content, this material shows good cell

adhesion property.<sup>[69]</sup> Adhesion of osteoblast cells (MC3TC) onto the scaffold surface was well observed under a microscope.

### 3.3. Packing Particles

2D micromodels can also be constructed by randomly packing particles, such as uniformly or multiple-sized glass beads, between transparent parallel plates.<sup>[70]</sup> This approach can also be extended to three dimensions, which more closely mimic the complexity of natural porous media, by densely packing glass beads in a quartz capillary having a square or a rectangular cross section. Depending on the bead size, the bead pack is sintered at 850–900 °C for 1–10 min to solidify the medium without destroying its original porous structure. By employing fluorescent fluids that have the same refractive index as the glass beads, one can visualize the 3D pore space structure and fluid flow within it using a confocal microscope, as shown in Figure 4g. The 3D structure of each phase can also be reconstructed from the confocal microscopy images. To date, this technique has been successfully applied to investigate the configuration of trapped fluid, the mobilization of nonwetting fluid, the breakup of nonwetting fluid, and the spatial fluctuations of fluid velocities in porous media.<sup>[10,28,71]</sup>

**Table 1** summarizes the features of the most widely used materials with relevance to micromodels, in terms of their optical, mechanical, thermal, and chemical properties, as well as the most common manufacturing methods. This information provides useful guidelines for selecting the proper material and manufacturing method for the micromodel study. Moreover, it is worth noting the difference of porous structure between consolidated rocks and unconsolidated soils; the former usually have lower porosity and permeability than the latter. This structural factor should also be considered when designing a micromodel along with other criteria on the operational conditions.

**Table 1.** Summary of the properties and the manufacturing methods for the common micromodel materials.

Material	Transparency <sup>[13]</sup>	Young's modulus [GPa]	Operational temperature range [°C]	Solvent compatibility	Water advancing contact angle [°] <sup>[15]</sup>	Wetting treatment	Commonest method of fabrication
Glass	Transparent (refractive index = 1.45–1.8 <sup>[78]</sup> )	50–90 <sup>[13]</sup>	<500 <sup>[77]</sup>	Compatible to most solvents <sup>[13]</sup>	25–35	Coating (gold) <sup>[19]</sup> Oxygen plasma <sup>[72]</sup> Silanization <sup>[18]</sup>	Lithography–etching Bead packing
Silicon	Transparent to UV	130–180 <sup>[13]</sup>	<1415 <sup>[15]</sup>	Compatible to most Solvents <sup>[13]</sup>	110	Silanization <sup>[18]</sup>	Lithography–etching
PDMS	Transparent (refractive index = 1.4 <sup>[33,79]</sup> )	0.0013–0.003 <sup>[32]</sup>	40–50 <sup>[77]</sup>	Incompatible to nonpolar solvents <sup>[37]</sup>	110	UV-initiated (poly (acrylic acid) graft patterning) <sup>[35]</sup> UV–ozone <sup>[73]</sup> Plasma oxidation <sup>[34,72]</sup> Polyelectrolyte multilayer coating <sup>[36b]</sup>	Soft lithography
PMMA	Transparent (refractive index = 1.492 <sup>[79]</sup> )	1.8–1.3 <sup>[40]</sup>	–70 to 100 <sup>[77]</sup>	Resistant to acids, bases (medium conc.), oil, petrol Nonresistant to alcohols, acetone, benzol <sup>[76]</sup>	60–75	Plasma treatment <sup>[44,74,77]</sup> UV/ozone exposure <sup>[45]</sup> Nitric acid oxidation <sup>[45]</sup> Polymer coating <sup>[45]</sup> Laser radiation <sup>[75]</sup>	Hot embossing 3D printing

## 4. Experiments and Results

Micromodels that combine advanced microscopy technology allow researchers to directly observe both static and dynamic conditions of fluid flow within the media, not only at the macroscale but also at the pore scale. This direct visualization is especially valuable for studying the flow involving two or more phases in porous media. In many cases, observations of pore-scale phenomena inspire hypotheses related to the underlying mechanisms and help to form qualitative and quantitative models. These theoretical interpretations usually result in predictions at the macroscale, which can then be compared with macroscale experimental results to support or disprove hypotheses.

The study of multiphase flow involving two or more fluids in porous media seeks to obtain data on two key pieces of information: the evolution of the interfaces between the fluids and the velocity field in each individual phase. The former can be either pore scale or macroscale. If the micromodel is 2D and, therefore, fluids flow in the same plane, the interface evolution can be straightforwardly observed by regular optical microscopes; sometimes dyes are added to one or more fluid phases to improve the visualization. In contrast, if the micromodel has a truly 3D structure in which light may be scattered or refracted at the fluid–solid or fluid–fluid interfaces, optical observation becomes more challenging. To overcome this problem, researchers match the refractive index of the fluids with that of the matrix material so that light can penetrate the media with minimal scattering from the interfaces. To obtain the 3D fluid structure, confocal laser scanning microscopy is used to scan the inner cross sections of the media, and enables the reconstruction of the 3D structure from stacks of planar images. **Figure 5** illustrates bright-field and fluorescent microscopy images from 2D micromodels,<sup>[31a,51]</sup> as well as the confocal images and reconstructed 3D structure from a 3D micromodel.<sup>[10]</sup> Moreover, information of the overall volume fraction of each individual phase can be easily obtained with the identified interface. The fluid velocity field, on the other hand, is most commonly studied using particle image velocimetry (PIV) or particle-tracking velocimetry (PTV), nonintrusive optical techniques for extracting flow characteristics by analyzing the motion of the seeded tracer particles.<sup>[80]</sup> We will discuss the

characterization of interface evolution and velocity field in more detail with examples in Sections 4.1 and 4.2, respectively.

Micromodels have also been used to study the flow–solid interaction in porous media, such as with flow-induced matrix deformation and microbial growth. In these cases, the direct observation of the motion or evolution of the solid phase is the key. We will discuss a few research examples in Section 4.3.

### 4.1. Fluid Structure and Interface Evolution

#### 4.1.1. Macroscale Visualization

The displacement of one fluid saturating the porous medium by another immiscible fluid is pervasive in many natural and engineering processes, such as during water infiltration into soil, EOR, and CO<sub>2</sub> sequestration. Although many applications would prefer a stable displacement front, in many cases the displacing phase invades along some preferential paths and generates finger-like structures. The fingering effect due to interfacial instability was extensively studied first in Hele-Shaw cells—thin chambers enclosed by two parallel plates—because the diffusive displacement in homogeneous porous media shares the same governing equations with that in the simple Hele-Shaw cell.<sup>[81]</sup> However, the structural and wettability heterogeneity inherent to natural porous media are difficult to recapitulate in a Hele-Shaw cell. Instead, the use of micromodels enables the investigations on the effects of wettability and heterogeneous pore structure. It has been shown that the displacement pattern in porous media depends on not only the viscosity ratio of the two fluids and the capillary number  $Ca = \mu V / \sigma$  (where  $\mu$ ,  $V$ , and  $\sigma$  are the dynamic viscosity, characteristic velocity, and interfacial tension, respectively),<sup>[71b,82]</sup> but also the wettability and the heterogeneity of the porous structure.<sup>[19,62b,83]</sup> It was found that increased wettability of the invading fluid could enhance displacement efficiency up to a critical contact angle; beyond that critical contact angle, the trend is reversed;<sup>[62b,84]</sup> the pore structure heterogeneity affects the invading structure due to the nonuniform capillary pressure threshold.<sup>[83]</sup> **Figure 6** shows the fingering structures in micromodels with various wettabilities and the comparison between fingering structures in heterogeneous media and homogeneous media. This information provides

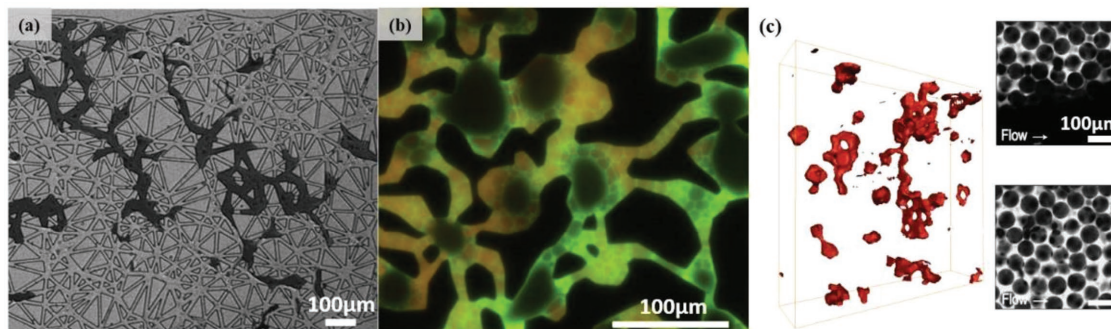


**Figure 5.** Microscopy images of the inner fluid structure in 2D and 3D micromodels. a) Optical microscopy image of ink-dyed water and fluorinert flowing through a PDMS-based micromodel. Reproduced with permission.<sup>[31a]</sup> Copyright 2013, American Geophysical Union. b) Fluorescent microscopy image of oil (orange)-in-water (green) emulsion and gas (dark brown located in the center of pores) flowing through a silicon-based micromodel. Reproduced with permission.<sup>[51]</sup> Copyright 2014, Elsevier. c) Confocal microscopy images of water (bright) invasion into oil saturated glass-bead packing, as well as the reconstructed 3D structure of the trapped oil blobs. Reproduced with permission.<sup>[10]</sup> Copyright 2013, American Institute of Chemical Engineers.



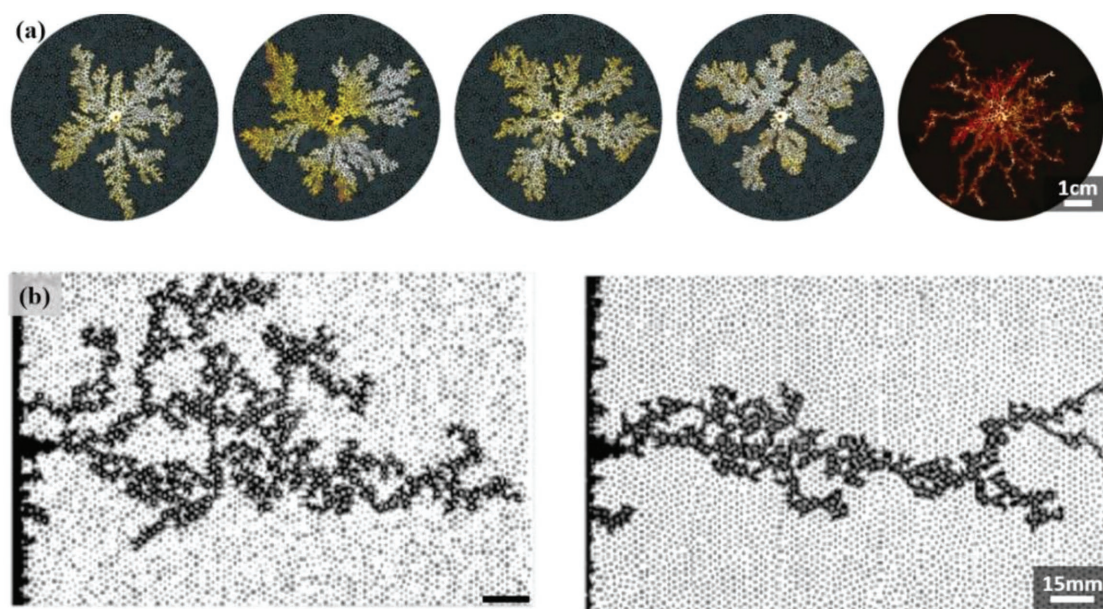


**Figure 6.** Microscopy images of the fingering structures of two-phase flow in micromodels. a) Fingering structures formed in imbibition inside a 2D irregular pillar micromodel with different wettability ranged from completely oil wet (left) toward completely water wet (right) at  $Ca = 2.9 \times 10^{-2}$ .<sup>[62b]</sup> b) Fingering patterns formed in drainage through hydrophilic porous media with heterogeneous porous structure (left) and homogeneous porous structure (right) at  $Ca = 8 \times 10^{-5}$ . Reproduced with permission.<sup>[83]</sup> Copyright 2015, American Geophysical Union.

important guidance on understanding and controlling the displacement patterns for multiphase flows in porous media. Moreover, micromodels allow for studying the effect of macroscale structural heterogeneity in porous media, such as fractures, on the invading pattern.<sup>[1b,e,50,51]</sup> These studies shed light on understanding the oil recovery in fractured reservoirs and the preferential flow in soil.

The microscopy images also enable the determination of the volume fraction of each individual phase in the micromodel, by assuming that the area occupation in the cross sections reflects the real volume occupation in the porous medium. In certain displacement processes, the variation of volume fraction is an important indicator of the displacement efficacy, such as the residual oil saturation in oil recovery and the residual fluid saturation in  $CO_2$  sequestration.<sup>[85]</sup>

#### 4.1.2. Pore-Scale Visualization

Pore-scale visualization can facilitate the clarification of multiphase flow mechanisms in porous media. One example is in the study of capillary trapping, which refers to the process wherein the nonwetting phase is trapped in the pore space, in the form of discrete blobs, by capillary forces. Capillary trapping appears in almost all porous media flow involving two or more immiscible phases, such as enhanced oil recovery and  $CO_2$  sequestration. Depending on the application, we may want to either minimize or maximize the capillary trapping of the discrete blobs. Studies conducted in micromodels dating back to the 1980s identified two primary capillary-trapping phenomena: bypass trapping due to the pore-scale heterogeneity of the flow resistance, and snap-off trapping due to the dynamic competition between capillary forces and viscous forces.<sup>[82b,86]</sup> **Figure 7a,b** demonstrates these two trapping

phenomena.<sup>[21c,86]</sup> In drainage, the wetting defending phase is mainly trapped by the bypass mechanism; in imbibition, however, the nonwetting defending phase can be trapped by either bypass or snap-off, or a combination of both mechanisms, depending on the local topology of the pore structure, the surface roughness, and the  $Ca$ .<sup>[21a,c,87]</sup> In general, surface roughness could enhance the snap-off trapping; bypass is more likely to be dominant at smaller  $Ca$ .<sup>[21c,88]</sup> Notably, using confocal microscopy on 3D index-matching micromodels one can directly visualize and characterize the full 3D structure of the trapped ganglia, as shown in Figure 7c.

Other examples of identifying multiphase flow mechanisms by pore-scale visualization include identifying the role of large cavities, or vugs, in varying the porosity–permeability relation and decreasing the displacement efficiency;<sup>[89]</sup> recognizing osmosis gradient as the oil mobilization mechanism in low-salinity water flooding EOR;<sup>[21b,90]</sup> examining the effect of spreading coefficient, a function of the interfacial tensions between any two phases, on the dual-displacement efficiency in three-phase flow in porous media, such as the tertiary gas flooding in oil recovery;<sup>[87b,c,91]</sup> demonstrating the effects of pore-scale fluid dynamics and viscosity on trapped fluid configuration within 3D micromodel;<sup>[10,71a]</sup> and inspecting foam-oil dynamics during foam flooding EOR.<sup>[31d,48,49,62a,85d,92]</sup> This information is of great importance to evaluating and developing new EOR methods.

#### 4.2. Flow Visualization

Micromodels also provide a platform that enables the direct flow visualization inside a porous medium. The most commonly applied method to retrieve the velocity field is micro-PIV ( $\mu$ -PIV) or micro-PTV ( $\mu$ -PTV).<sup>[3a,9c,e,93]</sup> By seeding micrometer-sized

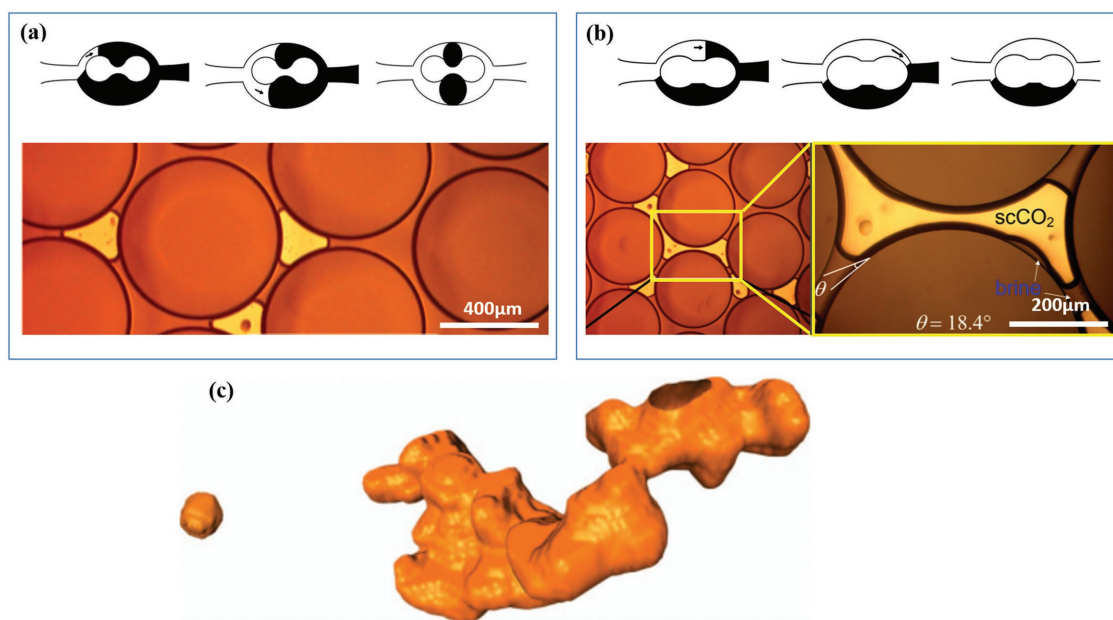


**Figure 7.** a) Schematics and microscopy image of bypass trapping of nonwetting ganglia. Reproduced with permission.<sup>[21c]</sup> Copyright 2017, American Geophysical Union. b) Schematics and microscopy images of snap-off trapping of nonwetting ganglia. Reproduced with permission.<sup>[21c]</sup> Copyright 2017, American Geophysical Union. c) 3D renderings of nonwetting oil ganglia from confocal microscopy images. Reproduced with permission.<sup>[71b]</sup> Copyright 2014, AIP Publishing LLC.

density-matched tracer particles into the fluid and assuming that the particles move along the flow streams without disturbing the flow, the particle velocity can be regarded as a faithful probe of the flow velocity. The particle motion is then visualized by obtaining images with short time intervals. In PIV, a high density of particles is employed, and the mean displacements of small interrogation areas in the flow are calculated using autocorrelation or cross-correlation techniques. Therefore, the mean velocity in each interrogation area can be determined based on the measured mean displacement over the imaging time interval. In PTV, a lower density of particles is employed, enabling the location of the same particles to be located in successive images. Therefore, the individual particle velocities can be

determined based on the individual particle displacements over the given time interval. Both PIV and PTV usually use fluorescent tracer particles and a high-resolution microscope (such as a confocal laser scanning microscope) to visualize the particle motion;<sup>[80,94]</sup> for 3D imaging, it is important to match the refractive index between the fluids and particles. The flow velocity field obtained using  $\mu$ -PIV from 2D silicon-based micromodel with an array of pillars by deep reactive ion etching and 3D glass bead-packed micromodels is shown in **Figure 8**.

A few examples of using PIV to facilitate understanding of the fluid flow in micromodels include quantifying turbulent flow through 3D porous media by measuring the mean velocity, the geometric length scale of the turbulent flow, and

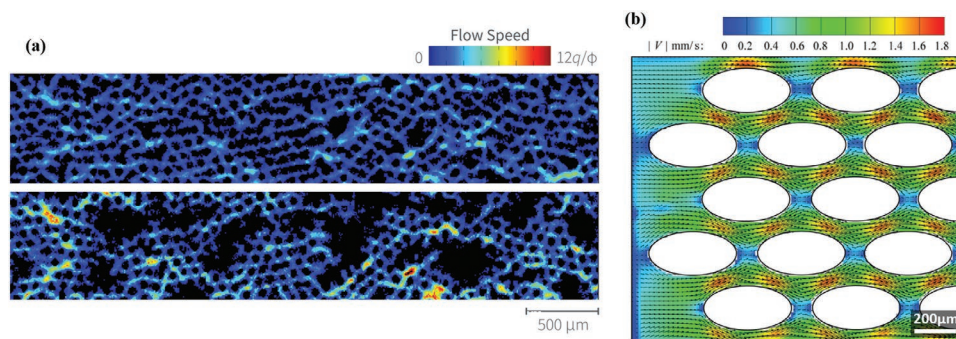


**Figure 8.** a) Map of flow velocity during single-phase flow (upper panel) and flow of fluid around trapped oil blobs (lower panel; blobs shown in black) inside a 3D glass-bead-packed micromodel. The flow velocity map was obtained by micro-PIV with 1 μm fluorescent latex microparticles as the tracer particles imaged by confocal microscopy. Adapted with permission.<sup>[28]</sup> Copyright 2013, American Physical Society. Color scale shows flow speeds ranging from 0 to  $12q/\phi$  where  $q$  is the imposed Darcy flow speed and  $\phi$  is the porosity. b) Average velocity field of CO<sub>2</sub> captured inside a silicon-based micromodel with regular array of pillars. The velocity field was obtained by micro-PIV with 1 μm fluorescent particles as the tracer particles imaged by FluoSpheres fluorescent microscopy. Reproduced with permission.<sup>[9e]</sup> Copyright 2015, Elsevier.

the turbulent Reynolds number;<sup>[93,95]</sup> quantifying both longitudinal and transverse velocity components for single- and multiphase flows through 3D porous media;<sup>[28,93h]</sup> characterizing the dynamics of CO<sub>2</sub> drainage at reservoir conditions of 80 bar and 24–40 °C;<sup>[9e]</sup> and tracking the formation and migration of interface during drainage and imbibition with two immiscible fluids.<sup>[93g]</sup> The velocity field obtained from  $\mu$ -PIV is also important for validating numerical simulations of the flow.<sup>[30a,93b]</sup>

#### 4.3. Fluid–Solid Interaction

When phase change occurs in porous media, the solid matrix would likely deform due to the pressure change. The deformation of the matrix will in turn influence the fluid flow in the interstitial space. For example, during wood drying, the loss of water sometimes induces wood cracking, collapse, or warping. This phenomenon was studied using a glass-based micromodel with a random structure characteristic of softwood. The experiment successfully captured “Haines jumps”—abrupt bursts in flow during the displacement of a wetting fluid by a nonwetting fluid—as seen by monitoring the sudden liquid redistribution during this process.<sup>[96]</sup> In another example, a 3D PDMS-based micromodel was developed to simulate and study the shrinkage of deformable porous media during drying, which is relevant to the food industry.<sup>[30c]</sup> The micromodel was fabricated by binding several layers of PDMS patterns by plasma cleaning and generating the perpendicular throats by laser perforation. The shrinkage profile was examined by measuring the distances between certain select points over time during the drying process. The shrinkage increases as the drying advances, consistent with the behavior of common biological materials.

Dissolution of the solid matrix in subsurface porous media flow occurs in many processes in the environmental engineering and petroleum industry. For example, during carbon sequestration, CO<sub>2</sub>-acidified formation water could change the porosity and permeability of the carbonate reservoir, and therefore the storage capacity and the long-term security of the well. In the acidizing enhanced oil recovery, acidified brine is injected into carbonate reservoirs to increase the porosity and permeability of the reservoir.<sup>[97]</sup> To capture the chemical interaction between the subsurface flow and the solid matrix, real rock-based micromodels have been recently developed to address this poorly understood problem. By etching flow channels in a natural calcite crystal substrate and binding with a glass, a micromodel was fabricated and then used to investigate the carbonate dissolution during acidic flows through the pore-scale visualization.<sup>[97]</sup> This study demonstrates the flow- and crystal-orientation-directed preferential dissolution and replicates the wormhole generation in acidizing processes. In another example, real rock–PDMS combined micromodel has also been developed for real-time tracking of subsurface reactive transport.<sup>[98]</sup>

As an opposite process of the matrix dissolution, formation of minerals and the subsequent precipitation to the solid matrix may also occur in subsurface porous media, such as the biomineralization. The growth of biofilm and the resultant CaCO<sub>3</sub> precipitation in porous media have been studied in a silicon-based micromodel covered with a thin layer of silicon dioxide created

by thermal oxidation.<sup>[99]</sup> The results implied that biomineralization could enhance the complexity of the flow paths, and likely affect the extent of transverse mixing, which may further influence the mineral precipitation.<sup>[99]</sup> In another example, the coupling of brucite dissolution and carbonate mineral precipitation was studied in an unsaturated glass micromodel under evaporative conditions; the results shed light on understanding the mineral–fluid reactions in Earth’s shallow subsurface.<sup>[100]</sup>

The study on the transport of particles, hard or soft, with flow through porous media is another example that significantly benefits from the micromodel technique. For example, flow of colloidal particle suspensions was carefully examined in PDMS-based micromodels with controllable surface roughness, particle–throat ratio, flow rate, and fluid salinity.<sup>[101]</sup> Pore-scale observations identified the distinct mechanisms of particle deposition on smooth and rough surfaces. The particle deposition at the pore scale through various identified mechanisms results in different colloid transport behaviors at the macroscale. This study validated and expanded the conventional filtration theory, which is important for understanding the relevant engineering processes, such as bioremediation. Moreover, micromodels have been used to study the transport of microgels through porous media, which sheds light on understanding gel treatments for EOR.<sup>[102]</sup>

PDMS-based micromodels have also been used to investigate the interaction between the microbial extracellular polymeric substances at the water–air interface and the matrix, which mimics the porous soil. The stabilization of the polymeric skin at the interface was recognized as the mechanism responsible for the alteration of moisture at the pore scale. This study helps our understanding on the influence of microbial activities on controlling soil moisture at the macroscale, which is critical for seedling survival and plant growth.<sup>[103]</sup>

#### 4.4. From Micro- to Nanofluidic Model Porous Media

The emerging unconventional oil and gas reservoirs, such as shale and tight gas sands, feature ultrasmall pore sizes on the order of 1–100 nm.<sup>[104]</sup> Under such a small length scale, continuous assumptions and Darcy’s law fail in describing the fluid flow behavior in the porous media. Instead, other flow mechanisms such as flow slippage start appearing. Thoroughly understanding the physics of flow behaviors in such nanoporous media is critical for enhancing the oil and gas production in these unconventional reservoirs. Moreover, flow in nanoporous media exists in many other natural and industrial systems such as water flow in plants and in synthesis of advanced materials.<sup>[105]</sup> To address this poorly understood problem, nanofluidic model porous media have been developed for studying the fluid flow and phase behavior in nanoscale pores. Fluidic networks containing channels with at least one dimension at the nanometer scale have been developed to study multiphase flow processes such as drying and imbibition.<sup>[106]</sup> Packed beds consisting of nanometer-sized silica particles have been developed to investigate capillary condensation.<sup>[107]</sup> Given the difficulty of direct visualization at the pore scale in these nanoporous media, 1D nanochannels represent another important model system for studying phase behaviors in nanopores such as



gas slippage, capillary filling, and imbibition.<sup>[108]</sup> Readers that are interested in learning more about the nanofluidic model porous media may refer to ref. [104] for an excellent review on this topic.

## 5. Conclusions and Outlook

Micromodel, microfluidic model porous medium, provide a powerful experimental platform that enables the direct visualization of the flow dynamics and fluid–solid interactions inside the medium at the pore scale. Since their development in the 1950s, they have been widely appreciated for studying multiphase flow in many engineering and natural processes, such as enhanced oil recovery, carbon sequestration, and water infiltration. Most existing micromodels consist of single-layer microfluidic channels with an arbitrary porous pattern. Mostly made of glass, silicon, and transparent polymers, like PDMS and PMMA, these 2D micromodels can be readily characterized using an optical microscope. Glass and silicon have excellent mechanical, thermal, and chemical properties suitable for a wide range of studies; however, the material processing—etching or laser engraving—is relatively complicated. PDMS, as another widely used micromodel material, is ideal for replicating fine structures by molding; however, the low stiffness and weak thermal and chemical resistance limit its applications. To better capture the physics associated with the porous connection in the third dimension, several types of 3D micromodels have also been developed, mostly by using multiheight molds, binding multilayer 2D porous patterns, 3D printing, or packing particles. To allow the light to penetrate deep into the medium, the refractive index of the fluids must match that of the solid matrix. Laser scanning microscopy can be then used to capture high-resolution images at specific depths; 3D structure of a thick-layer micromodel can also be reconstructed from a stack of images. Moreover, the recent advances in additive manufacturing provide another promising technique for making micromodels. Additive manufacturing has been used to fabricate 2D micromodels for studying displacement patterns of multiphase flow and to fabricate 3D porous polymeric scaffolds for visualizing the flow field in the interstitial space. In Sections 3 and 4 of this review, we discuss in detail the properties and fabrication methods for the materials that are commonly used to construct micromodels.

It is noteworthy that the achieved porous structures of 3D micromodels are very limited; fabrication of 3D micromodels with arbitrary porous structure is still an unsolved problem. Although this could be potentially addressed by 3D printing technology, high-resolution printing is still very challenging. Moreover, the options of the optically transparent printable materials, especially those with relatively strong mechanical properties, seem very limited. Therefore, how to fabricate 3D micromodels with high-resolution, realistic porous structures deserves more research efforts.

Micromodels are particularly useful in studying multiphase flow in porous media by disclosing the fluid structure at both the pore scale and the macroscale, as well as the flow velocity field. In many cases, our understanding on the flow mechanisms comes from the pore-scale phenomena. The

interpretation of the pore-scale phenomena usually results in predictions at the macroscale, which can then be compared with macroscale experimental results. In Section 4 of this review, we summarize some classical and contemporary studies using micromodels about investigating the flow mechanisms, and applying  $\mu$ -PIV to characterize and quantify single- and multiphase flow in porous media. Moreover, many real processes involve the interaction between the fluid and the solid phases, such as the drying, the transport of particle suspensions, and the growth and transport of active matters. We also discuss examples using micromodels to study these problems.

Although micromodels have been so far mainly used to address problems in the petroleum, geologic, and environmental engineering, they have attracted research attentions in other areas, such as the food and wood industries. More importantly, we would anticipate a wide application of polymeric micromodels in biomedical engineering, given the rapid advances in hydrogel synthesis and microfabrication, such as 3D printing and microfluidics technology. The unique mechanical and chemical properties of many biodegradable polymers, especially hydrogels, allow the resultant model porous media to mimic the realistic tissues in many ways. By using confocal microscopy one can directly visualize and characterize a variety of dynamic processes, including fluid flow, molecular diffusion, and cell migration, inside the porous media. The application of polymer- or hydrogel-based micromodels could significantly promote our understanding on the interstitial flow and transport processes in biological tissues, and therefore benefit many relevant medical and healthcare technology.

## Acknowledgements

J.F. acknowledges the support from The City College of New York and American Chemical Society Petroleum Research Fund (57496-DN19). S.S.D. acknowledges support from Princeton University. The work performed at Harvard University was supported by the AEC, the NSF (DMR-1708729) and the Harvard MRSEC (DMR-1420570).

## Conflict of Interest

The authors declare no conflict of interest.

## Keywords

complex fluids, microfluidics, micromodels, multiphase flow, porous media

Received: October 13, 2017

Revised: January 19, 2018

Published online:

- [1] a) M. J. Blunt, B. Bijeljic, H. Dong, O. Gharbi, S. Iglaier, P. Mostaghimi, A. Paluszny, C. Pentland, *Adv. Water Resour.* **2013**, 51, 197; b) A. Mehmani, S. Kelly, C. Torres-Verdin, M. Balhoff, presented at *Unconventional Resources Technology Conf.*, Austin, Texas, USA, July, **2017**; c) P. Hou, Y. Ju, F. Gao, J. Wang, J. He, *Int. J. Coal*

- Sci. Technol.* **2016**, 3, 351; d) J. Cui, T. Babadagli, *Colloids Surf., A* **2017**, 529, 346; e) M. Haghighi, B. Xu, Y. C. Yortsos, *J. Colloid Interface Sci.* **1994**, 166, 168.
- [2] a) T. Bultreys, W. De Boever, V. Cnudde, *Earth-Sci. Rev.* **2016**, 155, 93; b) N. K. Karadimitriou, S. M. Hassanizadeh, *Vadose Zone J.* **2012**, 11, 1.
- [3] a) S. Y. Yoon, J. W. Ross, M. M. Mench, K. V. Sharp, *J. Power Sources* **2006**, 160, 1017; b) E. Kjeang, R. Michel, D. A. Harrington, N. Djilali, D. Sinton, *J. Am. Chem. Soc.* **2008**, 130, 4000.
- [4] a) L. Cardoso, S. P. Fritton, G. Gailani, M. Benalla, S. C. Cowin, *J. Biomech.* **2013**, 46, 253; b) P. Vaupel, F. Kallinowski, P. Okunieff, *Cancer Res.* **1989**, 49, 6449; c) J. B. West, C. T. Dollery, A. Naimark, *J. Appl. Physiol.* **1964**, 19, 713; d) M. Sato, N. Sasaki, M. Ato, S. Hirakawa, K. Sato, K. Sato, *PLoS One* **2015**, 10, e0137301; e) J. Wu, Q. Chen, W. Liu, Z. He, J.-M. Lin, *TrAC, Trends Anal. Chem.* **2017**, 87, 19.
- [5] a) M. Gad-El-Hak, *J. Fluids Eng.* **1999**, 121, 5; b) Z.-Y. Guo, Z.-X. Li, *Int. J. Heat Mass Transfer* **2003**, 46, 149.
- [6] a) L. Luquot, O. Rodriguez, P. Gouze, *Transp. Porous Media* **2014**, 101, 507; b) C. Noiriell, P. Gouze, D. Bernard, *Geophys. Res. Lett.* **2004**, 31, L24603; c) P. Gouze, L. Luquot, *J. Contam. Hydrol.* **2011**, 120–121, 45.
- [7] a) R. T. Armstrong, A. Georgiadis, H. Ott, D. Klemin, S. Berg, *Geophys. Res. Lett.* **2014**, 41, 55; b) S. Berg, S. Oedai, H. Ott, *Int. J. Greenhouse Gas Control* **2013**, 12, 478; c) S. Berg, R. Armstrong, H. Ott, A. Georgiadis, S. A. Klapp, A. Schwing, R. Neiteler, N. Brussee, A. Makurat, L. Leu, F. Enzmann, J. O. Schwarz, M. Wolf, F. Khan, M. Kersten, S. Irvine, M. Stampanoni, *Petrophysics* **2014**, 55, 304; d) S. Berg, H. Ott, S. A. Klapp, A. Schwing, R. Neiteler, N. Brussee, A. Makurat, L. Leu, F. Enzmann, J.-O. Schwarz, M. Kersten, S. Irvine, M. Stampanoni, *Proc. Natl. Acad. Sci. USA* **2013**, 110, 3755.
- [8] a) B. Manz, L. F. Gladden, P. B. Warren, *AIChE J.* **1999**, 45, 1845; b) Y.-Q. Song, *Cem. Concr. Res.* **2007**, 37, 325; c) K. Ogawa, T. Matsuka, S. Hirai, K. Okazaki, *Meas. Sci. Technol.* **2001**, 12, 172.
- [9] a) M. Heshmati, M. Piri, *Langmuir* **2014**, 30, 14151; b) M. Sohrabi, A. Danesh, D. H. Tehrani, M. Jamiolahmady, *Transp. Porous Media* **2008**, 72, 351; c) S. Roman, C. Soulaire, M. A. Alsaud, A. Kovscek, H. Tchelepi, *Adv. Water Resour.* **2016**, 95, 199; d) O. Mohammadzadeh, N. Rezaei, I. Chatzis, *Energy Fuels* **2010**, 24, 6327; e) F. Kazemifar, G. Blois, D. C. Kyritsis, K. T. Christensen, *Adv. Water Resour.* **2016**, 95, 352.
- [10] A. T. Krummel, S. S. Datta, S. Münster, D. A. Weitz, *AIChE J.* **2013**, 59, 1022.
- [11] A. Chatenever, J. C. Calhoun Jr., *J. Pet. Technol.* **1952**, 4, 149.
- [12] J. W. Grate, R. T. Kelly, J. Suter, N. C. Anheier, *Lab Chip* **2012**, 12, 4796.
- [13] K. Ren, J. Zhou, H. Wu, *Acc. Chem. Res.* **2013**, 46, 2396.
- [14] F. Kazemifar, G. Blois, D. C. Kyritsis, K. T. Christensen, *Water Resour. Res.* **2015**, 51, 3017.
- [15] X. Zhang, S. J. Haswell, *MRS Bull.* **2006**, 31, 95.
- [16] P. N. Nge, C. I. Rogers, A. T. Woolley, *Chem. Rev.* **2013**, 113, 2550.
- [17] F. Javadpour, D. Fisher, *J. Can. Pet. Technol.* **2008**, 47, 10.
- [18] J. W. Grate, M. G. Warner, J. W. Pittman, K. J. Dehoff, T. W. Wietsma, C. Zhang, M. Oostrom, *Water Resour. Res.* **2013**, 49, 4724.
- [19] J. Murison, B. Semin, J.-C. Baret, S. Herminghaus, M. Schröter, M. Brinkmann, *Phys. Rev. Appl.* **2014**, 2, 034002.
- [20] C. Elosua, D. Lopez-Torres, M. Hernaez, I. R. Matias, F. J. Arregui, *Nanoscale Res. Lett.* **2013**, 8, 539.
- [21] a) H. Geistlinger, I. Atefi-Dadavi, H.-J. Vogel, *Transp. Porous Media* **2016**, 112, 207; b) S. B. Fredriksen, A. U. Rognum, K. Sandengen, M. A. Fernø, *Petrophysics* **2017**, 58, 28; c) R. Hu, J. Wan, Y. Kim, T. K. Tokunaga, *Water Resour. Res.* **2017**, 53, 6377.
- [22] a) C. Iliescu, K. Luck Tan, F. Tay, J. Miao, presented at *Int. Conf. on Materials for Advanced Technologies*, Suntec City, Singapore, July, **2005**; b) N. K. Karadimitriou, V. Joekar-Niasar, S. M. Hassanizadeh, P. J. Kleingeld, L. J. Pyrak-Nolte, *Lab Chip* **2012**, 12, 3413; c) S. Mohammadi, A. Maghzi, M. H. Ghazanfari, M. Masihi, A. Mohebbi, R. Kharat, *Energy Sources, Part A* **2013**, 35, 193.
- [23] a) Y. Kanda, K. Matsuda, C. Murayama, J. Sugaya, *Sens. Actuators, A* **1990**, 23, 939; b) S. Queste, R. Salut, S. Clatot, J. Y. Rauch, C. G. K. Malek, *Microsyst. Technol.* **2010**, 16, 1485.
- [24] Z.-X. Xiao, G.-Y. Wu, Z.-H. Li, G.-B. Zhang, Y.-L. Hao, Y.-Y. Wang, *Sens. Actuators, A* **1999**, 72, 46.
- [25] P. B. Allen, D. T. Chiu, *Anal. Chem.* **2008**, 80, 7153.
- [26] L. Chen, G. Luo, K. Liu, J. Ma, B. Yao, Y. Yan, Y. Wang, *Sens. Actuators, B* **2006**, 119, 335.
- [27] a) H. Wu, B. Huang, R. N. Zare, *Lab Chip* **2005**, 5, 1393; b) R. S. Lima, P. a. G. C. Leão, M. H. O. Piazzetta, A. M. Monteiro, L. Y. Shiroma, A. L. Gobbi, E. Carrilho, *Sci. Rep.* **2015**, 5, 13276.
- [28] S. S. Datta, H. Chiang, T. S. Ramakrishnan, D. A. Weitz, *Phys. Rev. Lett.* **2013**, 111, 064501.
- [29] a) D. S. Park, S. Bou-Mikael, S. King, K. E. Thompson, C. S. Willson, D. E. Nikitopoulos, presented at *Proc. ASME Int. Mechanical Engineering Congress and Exposition*, Houston, TX, USA, November, **2012**; b) G. S. Fiorini, G. D. M. Jeffries, D. S. W. Lim, C. L. Kuyper, D. T. Chiu, *Lab Chip* **2003**, 3, 158; c) D. S. Park, S. King, K. E. Thompson, C. S. Willson, D. E. Nikitopoulos, presented at *Proc. ASME Int. Mechanical Engineering Congress and Exposition*, Denver, CO, USA, November, **2011**; d) M. Auset, A. A. Keller, *Water Resour. Res.* **2004**, 40, W03503.
- [30] a) A. Campos Marin, T. Grossi, E. Bianchi, G. Dubini, D. Lacroix, *Ann. Biomed. Eng.* **2017**, 45, 1341; b) J. Upadhyay, D. S. Park, K. E. Thompson, D. E. Nikitopoulos, presented at *Proc. ASME Int. Mechanical Engineering Congress and Exposition*, Houston, TX, USA, November, **2015**; c) L. A. Segura, M. G. Fuentes, C. P. Urrutia, G. M. Badillo, presented at *XX Congresso Brasileiro de Engenharia Química*, Florianópolis, Santa Catarina, Brazil, October, **2014**; d) D. S. Park, J. Upadhyay, V. Singh, K. E. Thompson, D. E. Nikitopoulos, presented at *Proc. ASME Int. Mechanical Engineering Congress and Exposition*, Houston, TX, USA, November, **2015**.
- [31] a) N. K. Karadimitriou, M. Musterd, P. J. Kleingeld, M. T. Kreutzer, S. M. Hassanizadeh, V. Joekar-Niasar, *Water Resour. Res.* **2013**, 49, 2056; b) J. C. McDonald, G. M. Whitesides, *Acc. Chem. Res.* **2002**, 35, 491; c) N. K. Karadimitriou, P. Nuske, P. J. Kleingeld, S. M. Hassanizadeh, R. Helmig, *Lab Chip* **2014**, 14, 2515; d) K. Ma, R. Lontas, C. A. Conn, G. J. Hirasaki, S. L. Biswal, *Soft Matter* **2012**, 8, 10669.
- [32] I. D. Johnston, D. K. McCluskey, C. K. L. Tan, M. C. Tracey, *J. Microchem. Microeng.* **2014**, 24, 035017.
- [33] Z. Cai, W. Qiu, G. Shao, W. Wang, *Sens. Actuators, A* **2013**, 204, 44.
- [34] a) J. L. Fritz, M. J. Owen, *J. Adhes.* **1995**, 54, 33; b) H. Makamba, J. H. Kim, K. Lim, N. Park, J. H. Hahn, *Electrophoresis* **2003**, 24, 3607.
- [35] M. H. Schneider, H. Willaime, Y. Tran, F. Rezgui, P. Tabeling, *Anal. Chem.* **2010**, 82, 8848.
- [36] a) W.-A. C. bauer, M. Fischlechner, C. Abell, W. T. S. huck, *Lab Chip* **2010**, 10, 1814; b) H. Schmolke, S. Demming, A. Edlich, V. Magdanz, S. Büttgenbach, E. Franco-Lara, R. Krull, C.-P. Klages, *Biomechanics* **2010**, 4, 044113.
- [37] J. N. Lee, C. Park, G. M. Whitesides, *Anal. Chem.* **2003**, 75, 6544.
- [38] a) J. Verdu, *J. Macromol. Sci., Part A: Pure Appl. Chem.* **1994**, 31, 1383; b) L. C. Brinson, T. S. Gates, *Int. J. Solids Struct.* **1995**, 32, 827.
- [39] A. Shamsi, A. Amir, P. Heydari, H. Hajghasem, M. Mohtashamifar, M. Esfandiari, *Microsyst. Technol.* **2014**, 20, 1925.
- [40] Material Property Database—MIT, Material Properties: PMMA, <http://www.mit.edu/~6.777/matprops/pmma.htm> (accessed: October 2017).
- [41] a) Yoastseo Home—Pmma Online, <http://pmma-online.eu/> (accessed: October 2017) b) T. F. Scientific PMMA Chemical

- Properties Documents and Support, <https://www.thermofisher.com/search/results?query=PMMA%20chemical%20properties&focusarea=Search%20All> (accessed: October 2017).
- [42] a) S. J. Leigh, C. P. Purcell, J. Bowen, D. A. Hutchins, J. A. Covington, D. R. Billson, *Sens. Actuators, A* **2011**, 168, 66; b) Y. Mizukami, D. Rajniak, A. Rajniak, M. Nishimura, *Sens. Actuators, B* **2002**, 81, 202.
- [43] A. K. Au, W. Huynh, L. F. Horowitz, A. Folch, *Angew. Chem., Int. Ed.* **2016**, 55, 3862.
- [44] A. G. G. Toh, Z. F. Wang, S. H. Ng, presented at *Proc. of the IEEE Sym. on Design, Test, Integration and Packaging of MEMS/MOEMS (DTIP of MEMS & MOEMS)*, Nice, France, April, **2008**.
- [45] J. J. Shah, J. Geist, L. E. Locascio, M. Gaitan, M. V. Rao, W. N. Vreeland, *Electrophoresis* **2006**, 27, 3788.
- [46] Y. Xia, G. M. Whitesides, *Annu. Rev. Mater. Sci.* **1998**, 28, 153.
- [47] J. Beaumont, H. Bodiguel, A. Colin, *Soft Matter* **2013**, 9, 10174.
- [48] K. Osei-Bonsu, P. Grassia, N. Shokri, *J. Colloid Interface Sci.* **2017**, 490, 850.
- [49] H. Emami Meybodi, R. Kharrat, M. Nasehi Araghi, *J. Pet. Sci. Eng.* **2011**, 78, 347.
- [50] A. Soudmand-Asli, S. S. Ayatollahi, H. Mohabatkari, M. Zareie, S. F. Shariatpanahi, *J. Pet. Sci. Eng.* **2007**, 58, 161.
- [51] J. Gauteplass, K. Chaudhary, A. R. Kovscek, M. A. Fernø, *Colloids Surf., A* **2015**, 468, 184.
- [52] a) J. Garra, T. Long, J. Currie, T. Schneider, R. White, M. Paranjape, *J. Vac. Sci. Technol., A* **2002**, 20, 975; b) B. Balakrishnan, S. Patil, E. Smela, *J. Micromech. Microeng.* **2009**, 19, 047002.
- [53] C. Iliescu, B. Chen, J. Miao, *Sens. Actuators, A* **2008**, 143, 154.
- [54] D. C. S. Bien, P. V. Rainey, S. J. N. Mitchell, H. S. Gamble, *J. Micromech. Microeng.* **2003**, 13, S34.
- [55] C. V. Chrysikopoulos, C. C. Plega, V. E. Katzourakis, *J. Hazard. Mater.* **2011**, 198, 299.
- [56] K. Xu, T. Liang, P. Zhu, P. Qi, J. Lu, C. Huh, M. Balhoff, *Lab Chip* **2017**, 17, 640.
- [57] a) I. W. Rangelow, *Vacuum* **2001**, 62, 279; b) H. Jansen, H. Gardeniers, M. D. Boer, M. Elwenspoek, J. Fluitman, *J. Micromech. Microeng.* **1996**, 6, 14.
- [58] J. Roth, *Review and Status of Physical Sputtering and Chemical Erosion of Plasma Facing Materials*, Springer, Berlin **2005**.
- [59] K. Kawai, F. Yamaguchi, A. Nakahara, S. Shoji, presented at *14th Int. Conf. on Miniaturized Systems for Chemistry and Life Sciences*, Groningen, The Netherlands, October, **2010**.
- [60] a) C. Iliescu, F. E. H. Tay, presented at *Int. Semiconductor Conf., Sinaia, Romania, December*, **2005**; b) E. Metwalli, C. G. Pantano, *Nucl. Instrum. Methods Phys. Res., Sect. B* **2003**, 207, 21; c) J. H. Park, N. E. Lee, J. Lee, J. S. Park, H. D. Park, *Microelectron. Eng.* **2005**, 82, 119; d) K. R. Williams, K. Gupta, M. Wasilik, *J. Microelectron. Syst.* **2003**, 12, 761.
- [61] N. S. K. Gunda, B. Bera, N. K. Karadimitriou, S. K. Mitra, S. M. Hassanizadeh, *Lab Chip* **2011**, 11, 3785.
- [62] a) S. Xiao, *Master of Science*, Rice University, Houston, TX, **2016**; b) B. Zhao, C. W. Macminn, R. Juanes, *Proc. Natl. Acad. Sci. USA* **2016**, 113, 10251.
- [63] L. Peng, Y. Deng, P. Yi, X. Lai, *J. Micromech. Microeng.* **2014**, 24, 013001.
- [64] C. Friedrich, P. Coane, J. Goettert, N. Gopinathin, *Precis. Eng.* **1998**, 22, 164.
- [65] D. Crandall, G. Ahmadi, D. Leonard, M. Ferer, D. H. Smith, *Rev. Sci. Instrum.* **2008**, 79, 044501.
- [66] I. Zein, D. W. Hutmacher, K. C. Tan, S. H. Teoh, *Biomaterials* **2002**, 23, 1169.
- [67] I. Gibson, D. Shi, *Rapid Prototyping J.* **1997**, 3, 129.
- [68] X. Li, C. Wang, W. Zhang, Y. Li, *Mater. Lett.* **2009**, 63, 403.
- [69] J. Jansen, F. P. W. Melchels, D. W. Grijpma, J. Feijen, *Biomacromolecules* **2009**, 10, 214.
- [70] a) G. Løvoll, Y. Méheust, K. J. Måløy, E. Aker, J. Schmittbuhl, *Energy* **2005**, 30, 861; b) K. J. Måløy, L. Furuberg, J. Feder, T. Jøssang, *Phys. Rev. Lett.* **1992**, 68, 2161; c) O. I. Frette, K. J. Måløy, J. Schmittbuhl, A. Hansen, *Phys. Rev. E* **1997**, 55, 2969; d) R. Toussaint, G. Løvoll, Y. Méheust, K. J. Måløy, J. Schmittbuhl, *EPL* **2005**, 71, 583; e) Y. Méheust, G. Løvoll, K. J. Måløy, J. Schmittbuhl, *Phys. Rev. E* **2002**, 66, 051603; f) L. Furuberg, K. J. Måløy, J. Feder, *Phys. Rev. E* **1996**, 53, 966; g) K. T. Tallakstad, H. A. Knudsen, T. Ramstad, G. Løvoll, K. J. Måløy, R. Toussaint, E. G. Flekkøy, *Phys. Rev. Lett.* **2009**, 102, 074502; h) K. T. Tallakstad, G. Løvoll, H. A. Knudsen, T. Ramstad, E. G. Flekkøy, K. J. Måløy, *Phys. Rev. E* **2009**, 80, 036308.
- [71] a) S. S. Datta, J.-B. Dupin, D. A. Weitz, *Phys. Fluids* **2014**, 26, 062004; b) S. S. Datta, T. S. Ramakrishnan, D. A. Weitz, *Phys. Fluids* **2014**, 26, 022002.
- [72] S. Bhattacharya, A. Datta, J. M. Berg, S. Gangopadhyay, *J. Microelectromech. Syst.* **2005**, 14, 590.
- [73] Y. Berdichevsky, J. Khandurina, A. Guttman, Y. H. Lo, *Sens. Actuators, B* **2004**, 97, 402.
- [74] J. Chai, F. Lu, B. Li, D. Y. Kwok, *Langmuir* **2004**, 20, 10919.
- [75] a) J. Lawrence, L. Li, *Mater. Sci. Eng., A* **2001**, 303, 142; b) D. Waugh, J. Lawrence, presented at *Int. Congress on Applications of Lasers and Electro-Optics (ICALEO)*, Orlando, FL, USA, January, **2009**.
- [76] Datenblatt KERN, Polymethylmethacrylat (PMMA), <https://www.kern.de/cgi-bin/riweta.cgi?nr=2610&lng=1> (accessed: October 2017).
- [77] G. Y. Wiederschain, *Biochemistry* **2008**, 73, 1350.
- [78] a) *Handbook of Capillary and Microchip Electrophoresis and Associated Microtechniques*, 3rd ed, (Ed: J. P. Landers), Taylor & Francis Group LLC, Boca Raton, FL **2008**; b) I. H. Malitson, *J. Optical Society of America* **1965**, 55, 1205.
- [79] H. Becker, C. Gärtner, *Anal. Bioanal. Chem.* **2008**, 390, 89.
- [80] J. G. Santiago, S. T. Wereley, C. D. Meinhart, D. J. Beebe, R. J. Adrian, *Exp. Fluids* **1998**, 25, 316.
- [81] G. M. Homsy, *Annu. Rev. Fluid Mech.* **1987**, 19, 271.
- [82] a) R. Lenormand, C. Zarcane, *Transp. Porous Media* **1989**, 4, 599; b) R. Lenormand, C. Zarcane, A. Sarr, *J. Fluid Mech.* **1983**, 135, 337; c) R. Lenormand, E. Touboul, C. Zarcane, *J. Fluid Mech.* **1988**, 189, 165; d) R. Lenormand, C. Zarcane, *Phys. Chem. Hydro. J.* **1985**, 6, 497.
- [83] A. Ferrari, J. Jimenez-Martinez, T. L. Borgne, Y. Méheust, I. Lunati, *Water Resour. Res.* **2015**, 51, 1381.
- [84] M. Jung, M. Brinkmann, R. Seemann, T. Hiller, M. Sanchez de La Lama, S. Herminghaus, *Phys. Rev. Fluids* **2016**, 1, 074202.
- [85] a) H. Amani, *J. Pet. Sci. Eng.* **2015**, 128, 212; b) S. C. Cao, S. Dai, J. Jung, *Int. J. Greenhouse Gas Control* **2016**, 44, 104; c) H. Amani, *J. Surfactants Deterg.* **2017**, 20, 589; d) C. A. Conn, K. Ma, G. J. Hirasaki, S. L. Biswal, *Lab Chip* **2014**, 14, 3968.
- [86] I. Chatzist, N. R. Morrow, H. T. Lim, *Soc. Pet. Eng. J.* **1983**, 23, 311.
- [87] a) H. Geistlinger, I. Ataei-Dadavi, S. Mohammadian, H.-J. Vogel, *Water Resour. Res.* **2015**, 51, 9094; b) A. A. Keller, M. J. Blunt, A. P. V. Roberts, *Transp. Porous Media* **1997**, 26, 277; c) P. E. Oren, J. Billiotte, W. V. Pinczewski, *SPE Form. Eval.* **1992**, 7, 70.
- [88] H. Geistlinger, I. Ataei-Dadavi, *J. Colloid Interface Sci.* **2015**, 459, 230.
- [89] a) M. Wu, F. Xiao, R. M. Johnson-Paben, S. T. Retterer, X. Yin, K. B. Neeves, *Lab Chip* **2012**, 12, 253; b) W. Xu, J. T. Ok, F. Xiao, K. B. Neeves, X. Yin, *Phys. Fluids* **2014**, 26, 093102.
- [90] K. Sandengen, A. Kristoffersen, K. Melhuus, L. O. Jøssang, *SPEJ, Soc. Pet. Eng. J.* **2016**, 21, 1227.
- [91] a) M. I. J. Van Dijke, K. S. Sorbie, M. Sohrabi, D. Tehrani, A. Danesh, presented at *Proc.—SPE/DOE Symp. Improved Oil Recovery*, Tulsa, Oklahoma, April, **2002**; b) J. Gauteplass, H. N. Follesø, A. Graue, A. R. Kovscek, M. A. Fernø, presented at *European Symp. on Improved Oil Recovery*, St. Petersburg, Russia, April, **2013**.



- [92] a) D. J. Manlowe, C. J. Radke, *SPE Reservoir Eng.* **1990**, 5, 495; b) A. R. Kovscek, G. Q. Tang, C. J. Radke, *Colloids Surf., A* **2007**, 302, 251.
- [93] a) A. C. Marin, T. Grossi, E. Bianchi, G. Dubini, D. Lacroix, *Ann. Biomed. Eng.* **2017**, 45, 1341; b) B. D. Wood, S. V. Apte, J. A. Liburdy, R. M. Ziazi, X. He, J. R. Finn, V. A. Patil, *Adv. Water Resour.* **2015**, 85, 45; c) M. A. Northrup, T. J. Kulp, S. M. Angel, G. F. Pinder, *Chem. Eng. Sci.* **1993**, 48, 13; d) V. A. Patil, J. A. Liburdy, *Exp. Fluids* **2013**, 54, 1497; e) S. Saleh, J. F. Thovert, P. M. Adler, *Exp. Fluids* **1992**, 12, 210; f) P. Salipante, S. D. Hudson, J. W. Schmidt, J. D. Wright, *Exp. Fluids* **2017**, 58, 85; g) G. Blois, J. M. Barros, K. T. Christensen, *Microfluid. Nanofluid.* **2015**, 18, 1391; h) A. Y. L. Huang, M. Y. F. Huang, H. Capart, R.-H. Chen, *Exp. Fluids* **2008**, 45, 309; i) H. G. Maas, A. Gruen, D. Papantoniou, *Exp. Fluids* **1993**, 15, 133; j) N. A. Malik, T. Dracos, D. A. Papantoniou, *Exp. Fluids* **1993**, 15, 279; k) G. Blois, J. M. Barros, K. T. Christensen, presented at *Int. Symp. on Particle Image Velocimetry*, Delft, The Netherlands, July, **2013**; l) V. A. Patil, J. A. Liburdy, *Phys. Fluids* **2013**, 25, 043304.
- [94] K. Singh, H. Menke, M. Andrew, Q. Lin, C. Rau, M. J. Blunt, B. Bijeljic, *Sci. Rep.* **2017**, 7, 5192.
- [95] V. A. Patil, J. A. Liburdy, *Chem. Eng. Sci.* **2015**, 123, 231.
- [96] C. A. Oyarzun, L. A. Segura, *Drying Technol.* **2009**, 27, 14.
- [97] W. Song, T. W. d. Haas, H. Fadaei, D. Sinton, *Lab Chip* **2014**, 14, 4382.
- [98] R. Singha, M. Sivaguru, G. A. Fried, B. W. Fouke, R. A. Sanford, M. Carrera, C. J. Werth, *J. Contam. Hydrol.* **2017**, 204, 28.
- [99] R. Singha, H. Yoon, R. A. Sanford, L. Katz, B. W. Fouke, C. J. Werth, *Environ. Sci. Technol.* **2015**, 49, 12094.
- [100] A. L. Harrison, G. M. Dipple, W. Song, I. M. Power, K. U. Mayer, A. Beinlich, D. Sinton, *Chem. Geol.* **2017**, 463, 1.
- [101] M. Auset, A. A. Keller, *Water Resour. Res.* **2006**, 42, W12S02.
- [102] B. Bai, Y. Liu, J.-P. Coste, L. Li, *SPE Reservoir Eval. Eng.* **2007**, 10, 176.
- [103] J. Deng, E. P. Orner, J. F. Chau, E. M. Anderson, A. L. Kadilak, R. L. Rubinstein, G. M. Bouchillon, R. A. Goodwin, D. J. Gage, L. M. Shor, *Soil Biol. Biochem.* **2015**, 83, 116.
- [104] B. Bao, J. Riordon, F. Mostowfi, D. Sinton, *Lab Chip* **2017**, 17, 2740.
- [105] a) A. D. Stroock, V. V. Pagay, M. A. Zwieniecki, N. M. Holbrook, *Annu. Rev. Fluid Mech.* **2014**, 46, 615; b) C. J. Brinker, G. W. Scherer, *Sol-Gel Science*, Academic, New York, NY **1990**.
- [106] a) O. Vincent, D. A. Sessoms, E. J. Huber, J. Guioth, A. D. Stroock, *Phys. Rev. Lett.* **2014**, 113, 1; b) S. A. Kelly, C. Torres-Verdin, M. T. Balhoff, *Lab Chip* **2016**, 16, 2829.
- [107] J. Ally, S. Molla, F. Mostowfi, *Langmuir* **2016**, 32, 4494.
- [108] Q. Wu, B. Bai, Y. Ma, J. T. Ok, X. Yin, K. Neeves, *SPEJ, Soc. Pet. Eng. J.* **2014**, 19, 5.